

The filamentary internal structure of the 3C279 blazar jet

Antonio Fuentes (✉ afuentes@iaa.es)

Instituto de Astrofísica de Andalucía (CSIC) <https://orcid.org/0000-0002-8773-4933>

Jose Gomez

Instituto de Astrofísica de Andalucía - CSIC <https://orcid.org/0000-0003-4190-7613>

José María Martí

Universitat de València

Manel Perucho

Universitat de València

Guang-Yao Zhao

Instituto de Astrofísica de Andalucía (CSIC)

Rocco Lico

Instituto de Astrofísica de Andalucía (CSIC)

Andrei Lobanov

Max-Planck-Institute for Radio Astronomy

Gabriele Bruni

INAF—Istituto di Astrofisica e Planetologia Spaziali

Yuri Kovalev

Lebedev Physical Institute <https://orcid.org/0000-0001-9303-3263>

Andrew Chael

Princeton University

Kazunori Akiyama

Massachusetts Institute of Technology

Katherine Bouman

California Institute of Technology

He Sun

California Institute of Technology

Ilje Cho

Instituto de Astrofísica de Andalucía (CSIC)

Efthalia Traianou

Instituto de Astrofísica de Andalucía (CSIC)

Teresa Toscano

Instituto de Astrofísica de Andalucía (CSIC)

Rohan Dahale

Instituto de Astrofísica de Andalucía (CSIC)

Leonid Gurvits

Joint Institute for VLBI ERIC

Svetlana Jorstad

Boston University

Jae-Young Kim

Kyungpook National University

Alan Marscher

Boston University

Yosuke Mizuno

Shanghai Jiao Tong University

Eduardo Ros

Max-Planck-Institut für Radioastronomie

Tuomas Savolainen

Aalto University

Physical Sciences - Article

Keywords:

Posted Date: March 23rd, 2022

DOI: <https://doi.org/10.21203/rs.3.rs-1449452/v1>

License:   This work is licensed under a Creative Commons Attribution 4.0 International License.

[Read Full License](#)

The filamentary internal structure of the 3C 279 blazar jet

Antonio Fuentes^{1,*}, José L. Gómez¹, José M. Martí^{2,3}, Manel Perucho^{2,3}, Guang-Yao Zhao¹, Rocco Lico^{1,4}, Andrei P. Lobanov^{5,6}, Gabriele Bruni⁷, Yuri Y. Kovalev^{8,6,5}, Andrew Chael^{9,10}, Kazunori Akiyama^{11,12,13}, Katherine L. Bouman¹⁴, He Sun¹⁴, Ilje Cho¹, Efthalia Traianou¹, Teresa Toscano¹, Rohan Dahale^{1,15}, Leonid I. Gurvits^{16,17}, Svetlana Jorstad^{18,19}, Jae-Young Kim^{20,21,5}, Alan P. Marscher¹⁸, Yosuke Mizuno^{22,23,24}, Eduardo Ros⁵, Tuomas Savolainen^{5,25,26}

¹Instituto de Astrofísica de Andalucía (CSIC), Glorieta de la Astronomía s/n, 18008 Granada, Spain

²Departament d’Astronomia i Astrofísica, Universitat de València, C/ Dr. Moliner, 50, E-46100 Burjassot, València, Spain

³Observatori Astronòmic, Universitat de València, C/ Catedràtic José Beltrán 2, E-46980 Paterna, València, Spain

⁴INAF—Istituto di Radioastronomia, via Gobetti 101, I-40129 Bologna, Italy

⁵Max-Planck-Institut für Radioastronomie, Auf dem Hügel 69, D-53121 Bonn, Germany

⁶Moscow Institute of Physics and Technology, Institutsky per. 9, Dolgoprudny, Moscow region, 141700, Russia

⁷INAF—Istituto di Astrofisica e Planetologia Spaziali, via Fosso del Cavaliere 100, I-00133 Roma, Italy

⁸Lebedev Physical Institute of the Russian Academy of Sciences, Leninsky prospekt 53, 119991 Moscow, Russia

⁹Princeton Center for Theoretical Science, Princeton University, Jadwin Hall, Princeton, NJ 08544, USA

¹⁰NASA Hubble Fellowship Program, Einstein Fellow

¹¹Massachusetts Institute of Technology Haystack Observatory, 99 Millstone Road, Westford, MA 01886, USA

¹²National Astronomical Observatory of Japan, 2-21-1 Osawa, Mitaka, Tokyo 181-8588, Japan

¹³Black Hole Initiative at Harvard University, 20 Garden Street, Cambridge, MA 02138, USA

¹⁴California Institute of Technology, 1200 East California Boulevard, Pasadena, CA 91125, USA

¹⁵Indian Institute of Science Education and Research Kolkata, Mohanpur, Nadia, West Bengal 741246, India

¹⁶Joint Institute for VLBI ERIC (JIVE), Oude Hoogeveensedijk 4, 7991 PD Dwingeloo, The Netherlands

¹⁷Aerospace Faculty, Delft University of Technology, Kluyverweg 1, 2629 HS Delft, The Netherlands

¹⁸Institute for Astrophysical Research, Boston University, 725 Commonwealth Avenue, Boston, MA 02215, USA

¹⁹Astronomical Institute, St. Petersburg State University, Universitetskij, Pr. 28, Petrodvorets, St. Petersburg 198504, Russia

²⁰Department of Astronomy and Atmospheric Sciences, Kyungpook National University, Daegu 702-701, Republic of Korea

²¹Korea Astronomy and Space Science Institute, 776 Daedeok-daero, Yuseong-gu, Daejeon 34055, Republic of Korea

²²Tsung-Dao Lee Institute, Shanghai Jiao Tong University, Shengrong Road 520, Shanghai, 201210, People’s Republic of China

²³School of Physics and Astronomy, Shanghai Jiao Tong University, 800 Dongchuan Road, Shanghai, 200240, People’s Republic of China

²⁴Institut für Theoretische Physik, Goethe-Universität at Frankfurt, Max-von-Laue-Straße 1, D-60438 Frankfurt am Main, Germany

²⁵Aalto University Metsähovi Radio Observatory, Metsähovintie 114, FI-02540 Kylmälä, Finland

²⁶Aalto University Department of Electronics and Nanoengineering, PL15500, FI-00076 Aalto, Finland

1 Supermassive black holes at the centre of active galactic nuclei power some of the most luminous
2 objects in the Universe¹. Typically, very long baseline interferometric (VLBI) observations of blazars
3 have revealed only funnel-like morphologies with little information of the ejected plasma internal
4 structure^{2,3}. Here we show extremely-high angular resolution images of the blazar 3C 279 obtained
5 with the space VLBI mission *RadioAstron*⁴, which allowed us to resolve the jet transversely and
6 reveal several filaments produced by Kelvin–Helmholtz instabilities in a kinetically dominated flow
7 that originate from the VLBI core and extend up to 175 parsecs (de-projected) downstream the jet.
8 The VLBI core appears to be elongated, in agreement with recent Event Horizon Telescope results⁵,
9 but thanks to our higher dynamic range and increased field of view we are able to connect the
10 immediate environment of the supermassive black hole with the large-scale jet. From the observed
11 linear polarization and strong cross-section emission asymmetry we can infer that the filaments are
12 threaded by a helical magnetic field rotating clockwise, as seen in the direction of the flow motion,
13 with an intrinsic helix pitch angle of $\sim 45^\circ$ in a jet with a Lorentz factor of ~ 13 .

14 Located at a redshift of $z = 0.536$ ⁶ in the Virgo con-
15stellation, the blazar 3C 279 is one of the most studied
16active galactic nuclei (AGN)^{7,8,9}. The powerful radio-
17jet emanating from its core was one of the first where
18apparent superluminal motions were reported^{10,11}, as
19well as one of the first where high-energy γ -ray emis-
20sion was detected¹². It has been the target of exten-
21sive centimetre and millimetre very long baseline inter-
22ferometric (VLBI) observations and monitoring cam-
23paigns^{2,13,14}, being the latest findings at millimetre
24wavelengths achieved by the Event Horizon Telescope
25(EHT) Collaboration⁵. We observed 3C 279 on 10

26 March 2014 at 22 GHz (1.3 cm) with the space VLBI
27mission *RadioAstron*⁴, a 10-m space radio telescope
28(SRT) on board of the *Spektr-R* satellite, and an array
29of 23 ground-based radio telescopes spanning baselines
30distances from hundreds of kilometers to the Earth di-
31ameter. The large number of detections reported within
32the *RadioAstron* AGN survey program¹⁵ made 3C 279
33an ideal target for detailed imaging.

34 Fig. 1 presents our *RadioAstron* space VLBI polari-
35metric image of the blazar 3C 279. A representative
36image reconstruction obtained using novel regularized
37maximum likelihood methods^{17,18} is shown along with

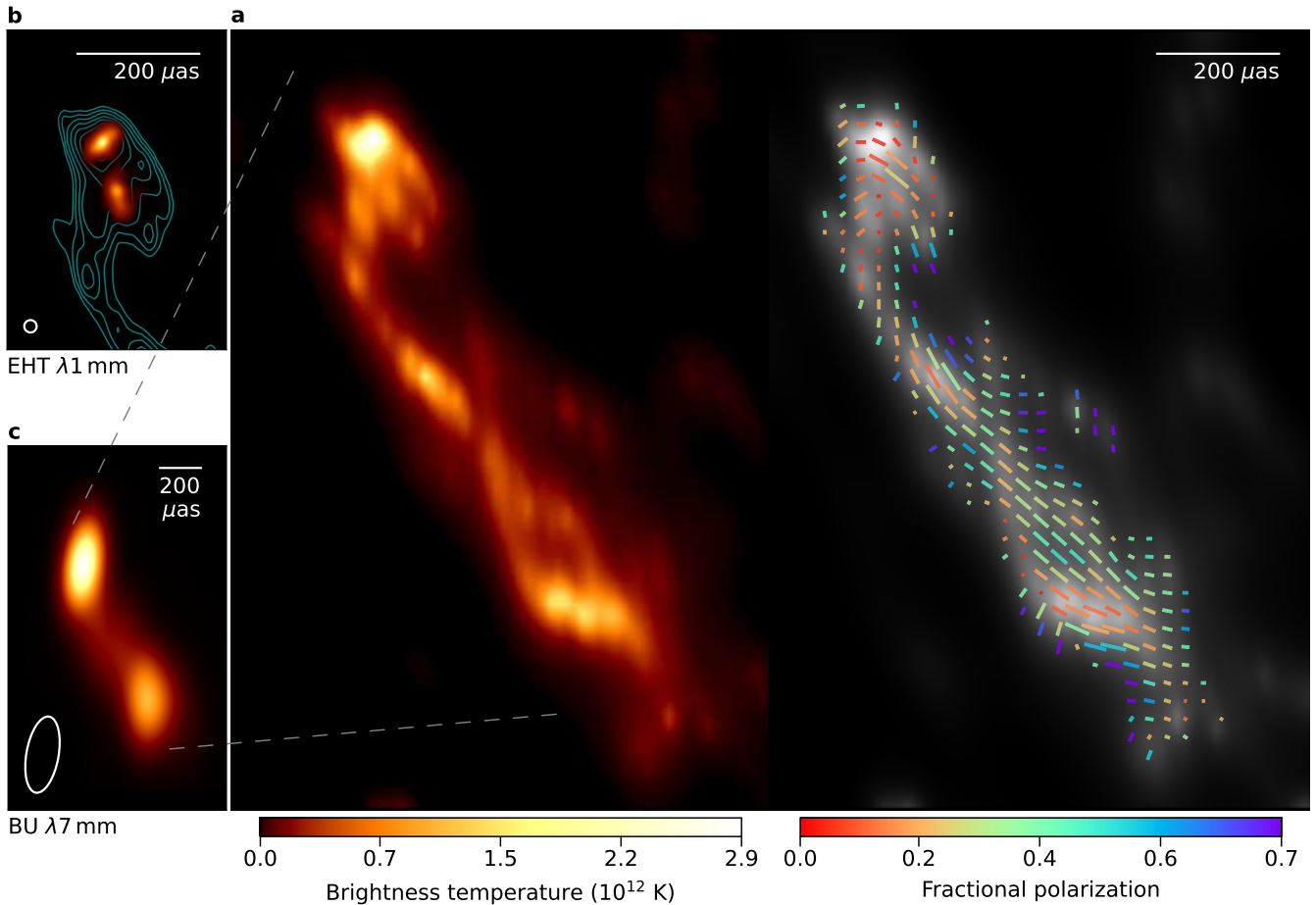


Figure 1: The filamentary structure of the jet in 3C 279 revealed by *RadioAstron*. **a**, Total intensity (left) and linearly polarized (right) *RadioAstron* image at 1.3 cm obtained on 10 March 2014. While both left and right images in **a** show brightness temperature in colour scale, the image on the right shows as well the recovered electric vector position angle overplotted as ticks. Their length and colour are proportional to the level of linearly polarized intensity and fractional polarization, respectively. **b**, The 1:1 scale 1.3 mm EHT image obtained in April 2017. Contours correspond to our *RadioAstron* image, which are shown to compare the different scales probed. Both images were aligned with respect to the pixel with maximum brightness. **c**, The 7 mm VLBA-BU-BLAZAR program image obtained on 25 February 2014. White ellipses at the bottom-left corner of **b** and **c** indicate the $20 \times 20 \mu\text{as}$ and $150 \times 360 \mu\text{as}$ convolving beams, respectively. Bottom colour bars refer only to information displayed on **a**.

38 the closest in time 7 mm VLBA-BU-BLAZAR program
 39 image obtained on 25 February 2014, and the 1.3 mm
 40 EHT image obtained in April 2017. We show a field
 41 of view of around 1×1 milliarcseconds (mas) with an
 42 image total flux density of 27.16 Jy, and note that all
 43 extended emission outside this region is resolved out by
 44 *RadioAstron*. The robustness of our image is demon-
 45 strated in Extended Data Fig. 2, where we show how it
 46 fits the data used for both total intensity and linearly
 47 polarized image reconstruction. We acknowledge how-
 48 ever that VLBI imaging is an ill-posed problem, and
 49 there is not an unique image reconstruction fitting the
 50 data (e.g. see the comprehensive image analysis carried
 51 out in ref. 19). The image in Fig. 1 is complemented by
 52 the 48 images presented in Extended Data Fig. 3 (see
 53 [Methods](#)).

54 The highly eccentric elliptical orbit of the SRT, with
 55 an apogee of $\sim 350\,000$ km, provided us with success-
 56 ful ground-space fringe detections of the source up to
 57 a projected baseline distance of 8 Earth’s diameters,
 58 probing a wide range of spatial frequencies perpendicu-

59 lar to the jet propagation direction (see Extended Data
 60 Fig. 1). At the longest projected baselines to *RadioAstron*,
 61 we achieve a resolving power of 27 microarcsec-
 62 onds (μas) at an observing wavelength of 1.3 cm, simi-
 63 lar to that obtained by the EHT at 1.3 mm ($\sim 20 \mu\text{as}$).
 64 Contrary to the EHT sparse sampling of the Fourier
 65 plane^{5,20}, the ground array supporting our space-VLBI
 66 observations provided a significantly larger filling frac-
 67 tion, which enabled us to reconstruct images with a dy-
 68 namic range two orders of magnitude larger than that
 69 achieved by the EHT. These key features of our image
 70 directly link both the high-resolution EHT images of
 71 the core at 1.3 mm and the low-resolution VLBA-BU-
 72 BLAZAR images of the extended jet at 7 mm.

73 In contrast to the contemporaneous 7 mm and clas-
 74 sical centimetre-wave VLBI jet images³, where the ob-
 75 served synchrotron emission seems to be contained in
 76 a funnel with a uniform cross section, we show in great
 77 detail the internal structure of a blazar jet and find
 78 strong evidence of the filamentary nature of the emit-
 79 ting regions within it. We identify the jet core as the

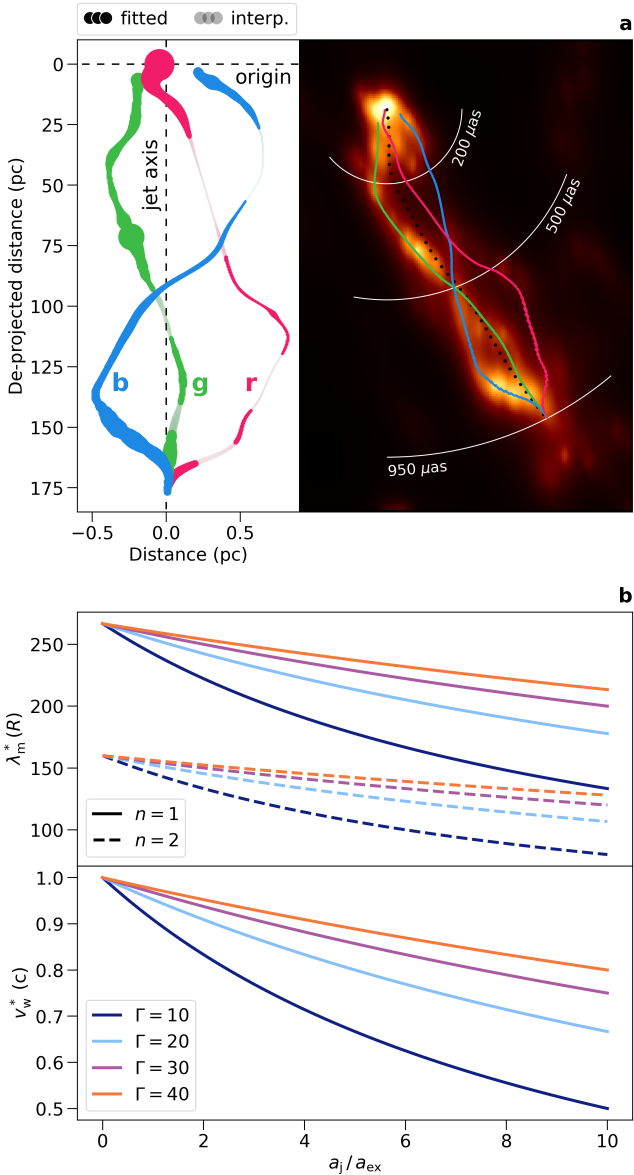


Figure 2: Analysis of the recovered filamentary structure. **a**, Left: de-projected filament coordinates fitted using three Gaussian curves (see Methods). Dimmer points indicate regions where the coordinates have been interpolated. Marker size scales with the flux density. Note the scales in the x- and y-axis are different. Right: position of the fitted filaments on top of the reconstructed image. **b**, Kelvin-Helmholtz instability mode wavelength (λ_m^*) and wave velocity (v_w^*) as a function of the jet and external medium sound speed ratio (a_j/a_{ex}). In addition to different Lorentz factor (Γ) values (line colour) within the range estimated in ref. ¹⁶, the top panel presents the results for both helical ($n = 1$) and elliptical ($n = 2$) instability surface modes (solid and dashed lines, respectively).

upstream bright component, and the so-called ‘core region’ encompasses the inner $\sim 200 \mu\text{as}$, roughly the extension of the features probed by the EHT. The base is slightly elongated and tilted in the southeast-northwest direction, from which several filaments emanate perpendicularly from it. In the top panel of Fig. 2 we show the de-projected¹ and relative right-ascension and dec-

¹For a redshift $z = 0.536$ ⁶, a viewing angle $\theta = 1.9^\circ$ ¹⁴, and a cosmology $H_0 = 67.7 \text{ km s}^{-1} \text{ Mpc}^{-1}$, $\Omega_m = 0.307$, and $\Omega_\Lambda =$

87 lination coordinates of the two main (hereinafter g and
88 b), and possibly third (r), filaments obtained from the
89 fitting of three Gaussian curves to transverse cuts to the
90 main jet axis (see Methods). Downstream of the core
91 region, the filament g is continuously recovered and con-
92 tains most of the eastern extended structure flux den-
93 sity. Initially propagating in the southern direction, it
94 displays a sharp bend of $\sim 45^\circ$ to the west, close to the
95 core region boundary. Although not continuously, we
96 are also able to reconstruct the filament b beyond the
97 inner $200 \mu\text{as}$ in what seems to be a helical-like mor-
98 phology. These two filaments converge at $\sim 500 \mu\text{as}$
99 downstream the jet, where the filament b crosses over g.
100 Further downstream, they bend and converge again at
101 $\sim 950 \mu\text{as}$, where the brightness of the weaker filament
102 is largely enhanced as it bends, dominating now the
103 reconstructed emission in the southernmost jet region.
104 Some diffuse emission is also systematically recovered
105 parallel to the filament g after the first crossing, which
106 might indicate the presence of a third filament (r).

The apparent perpendicular jet-base structure recon-
107 structed was also reported by the EHT Collaboration
108 in ref. ⁵. While we can recover up to three different fila-
109 ments emanating from the jet base, the EHT could only
110 recover one and is completely blind to the extended, fila-
111 mentary structure, primarily due to the lack of short-
112 spacing baselines. If aligned with respect to the bright-
113 ness peak, both images match remarkably well, and the
114 jet feature observed at 1.3 mm is coincident in position
115 and extension with our central filament. Within our
116 uncertainty, we do not appreciate a significant change
117 in the core position angle with respect to the EHT im-
118 age, taken three years apart. The single-epoch results
119 presented here do not allow us to discern whether this
120 elongated structure corresponds to the accretion disk or
121 to other extended jet component. Nonetheless, based
122 on the small viewing angle inferred¹⁴ ($\theta \sim 1.9^\circ$) and the
123 multi-epoch kinematic analysis of the model-fitted jet
124 components, ref. ⁵ opened the possibility for this struc-
125 ture to correspond to a highly bent part of the inner
126 jet.

Based on the aforementioned Gaussian fitting to the
128 observed filaments, we estimate an approximate spatial
129 periodicity λ_m of $950 \mu\text{as}$ (projected on the plane of
130 the sky) or 175 pc (de-projected), which corresponds
131 to $\sim 2.3 \times 10^6$ gravitational radii assuming a black
132 hole mass of $M_{\text{BH}} \simeq 8 \times 10^8 M_\odot$ ²². The possibility
133 for these filaments to reflect a fundamental periodicity
134 of the black hole or inner accretion disk directly
135 associated with their rotation should be dismissed, as
136 it would imply propagation speeds along the filaments
137 larger than the speed of light by orders of magnitude.
138 At the same time, explaining such a fundamental peri-
139 odicity in terms of precession of a jet nozzle, caused
140 by the Lense-Thirring effect²³ or a supermassive black
141 hole binary system, invoked to explain a sharp bend in
142 the nuclear region, have been recently discarded⁵. On
143 the other hand, anchoring the filaments to the outer
144 accretion disk to allow for a subluminal propagation
145 of the helical pattern would imply a exceedingly large

0.693²¹

(Keplerian) disk radius, that is, larger than ~ 1 light-year, about two orders of magnitude larger than the expected disk sizes²⁴.

According to ref.⁵, the jet no longer accelerates beyond $\sim 100 \mu\text{s}$ from the core, suggesting a kinetically dominated flow in which the observed filaments show a magnetic field structure dominated by the toroidal component (see the discussion in the next paragraph). Taking this into account, we conclude that these bright filaments reveal compressed regions with enhanced gas and magnetic pressure – favouring an increased synchrotron emissivity. Thus, these might be associated to the triggering and development of flow instabilities. Current-driven kink or Kelvin-Helmholtz (KH) instabilities are the most plausible mechanisms capable of developing such helical structures^{25,26,27}. Current-driven instabilities dominate in Poynting-flux regimes with strong helical magnetic fields, that is, in the jet’s acceleration and collimation region. On the contrary, KH instabilities have the largest growth in kinetically dominated flows, thus favored in our case. The extension of the filaments greatly exceeds the jet radius, which is expected for KH surface modes. While two filaments could be generated by an elliptical mode, the possible third filament observed might indicate the presence of an additional helical mode interfering with the elliptical.

Based on the most conservative estimations of the flow Lorentz factor in 3C 279¹⁶ ($\Gamma \in [10, 40]$) and assuming the jet is kinetically dominated and relatively cold, as expected for powerful jets already expanded and accelerated, the fastest growing frequency of a mode is given by $\omega_{nm}^* R/a_{\text{ex}} = (n + 2m + 1/2)\pi/2$ ^{28,29}, where R is the radius, a_{ex} the sound speed of the ambient medium, and n and m the type of mode ($n = 1, 2$ for helical and elliptical modes, respectively; and $m = 0$ for a surface mode). Taking $\omega \leq 2\pi c/\lambda_m$, we find $a_{\text{ex}} \simeq 10^{-2}c$ for both the helical and elliptical modes. At this maximum growth frequency, and for a highly supersonic jet (i.e. with jet Mach number $M_j \gg 1$), the wavelength of the mode and wave velocity are given, respectively, by

$$\lambda_m^* \simeq \frac{4}{n + 1/2} M_{\text{ex}} \frac{\Gamma}{a_j/a_{\text{ex}} + \Gamma} R \quad \text{and} \quad (1)$$

$$v_w^* \simeq \frac{\Gamma}{a_j/a_{\text{ex}} + \Gamma} u, \quad (2)$$

where M_{ex} is the Mach number of the jet with respect to the ambient sound speed ($M_{\text{ex}} \simeq c/a_{\text{ex}} \simeq 100$), a_j is the sound speed of the jet flow, and u is the jet flow velocity (which approximates the light speed c given the large Lorentz factors considered). With Eqs. 1 and 2, we can derive λ_m^* and v_w^* as a function of Γ and the ratio a_j/a_{ex} (see the bottom panel of Fig. 2). Based on these relations, our estimate for the ambient medium sound speed $a_{\text{ex}} \simeq 10^{-2}c$ and our assumption for the jet Mach number $M_j \gg 1$ are perfectly compatible with the condition $\lambda_m \geq \lambda_m^*$ (with $\lambda_m \simeq 175 \text{ pc}$) for the range $a_j \simeq 0.01 - 0.1c$ (which sets $M_j \geq 10$), also validating our assumption of a kinetically dominated flow at the observed scales. In the case of a dominating helical instability, the bottom panel of Fig. 2 shows that jet flow

Lorentz factors $\Gamma \leq 20$ are favoured by our analysis.

The analysis of the linearly polarized emission captured by *RadioAstron* and the supporting ground array reveals clear signatures of a toroidal magnetic field threaded to the relativistic jet. The source is midly polarized, with an integrated degree of linear polarization of $\sim 10\%$. The electric vector position angle, plotted as ticks of variable orientation, size, and colour in Fig. 1, traces the electric field direction along the jet, thus indicating a magnetic field predominantly perpendicular to the flow propagation direction, that is, consistent with a helical magnetic field dominated by its toroidal component. The core region is significantly depolarized and presents a more complicated polarization pattern, although we can distinguish two predominant orientations of the polarization angle. Departing from the centre–westernmost side of the core, the magnetic field seems to follow the filaments b and r, whereas from the easternmost side of the jet base, it seems to follow the filament g, until both orientations converge and stay aligned with the main jet axis. When downgraded to the same, lower resolution as that probed by the VLBA-BU-BLAZAR program, the polarization patterns obtained for the 7 mm and our *RadioAstron* image are remarkably similar. An observed field predominantly toroidal along the filaments, as indicated by the distribution of polarization vectors, is in agreement with the expected field structure beyond the collimation and acceleration region, in terms of conservation of the magnetic flux. The fact that no aligned component is observed indicates that the filaments lie inside the outer, sheared jet layers.

Relativistic magneto-hydrodynamic simulations of jets at parsec scales have shown that, in the presence of a helical magnetic field, the observed synchrotron emission is unevenly distributed across the jet width^{30,31,32,33}. Since the synchrotron radiation coefficients are a function of the angle between the magnetic field and the line of sight in the fluid frame, for a fixed viewing angle and jet flow velocity, the bulk of the emission will be located on either side of the main jet axis depending on the magnetic field helical pitch angle. This asymmetry is maximized when the helical magnetic field pitch angle (in the fluid frame) ϕ' equals to 45° (ref.³⁰). Given the strong asymmetry in the reconstructed emission between the eastern and western sides of the jet axis, we can assume that the viewing angle in the fluid’s frame approximates ϕ' , that is $\theta' \simeq \phi'$. Hence, given the inferred viewing angle in the observer’s frame ($\theta \sim 1.9^\circ$) (ref.¹⁴) and the light aberration transformation³⁴, we can infer a jet bulk flow Lorentz factor of $\Gamma \simeq 13$, which is in excellent agreement with the estimates provided by analyzing the kinematics of the parsec-scale jet¹⁴, and satisfies the upper limit previously established by our KH instability analysis. Moreover, this allows us to estimate the viewing angle θ_r at which the emission asymmetry will reverse from one side to the other as $\cos \theta_r = (1 - 1/\Gamma^2)^{1/2}$ (ref.³⁰), which results in $\theta_r \simeq 4.4^\circ$ for $\Gamma = 13$. Since $\theta < \theta_r$ and the bulk of the reconstructed emission is located to the east of the jet axis, we infer a helical magnetic field rotating

clockwise as seen in the direction of flow motion. The Lorentz-transformation of the magnetic field from the fluid’s to the observer’s frame boosts the toroidal component by Γ (ref. ³⁵), and therefore the helix pitch angle transforms as $\tan \phi = \Gamma \tan \phi'$. This makes $\phi \simeq 86^\circ$ in the observer frame, which is in agreement with the predominantly toroidal magnetic field observed.

The findings presented in this paper, supported as well by previous VSOP (e.g. ref. ³⁶) and *RadioAstron* (e.g. refs. ^{37,38}) space VLBI observations, strongly suggest that blazar jets have a complex and rich internal structure beyond the funnel-like morphologies reported by ground-based VLBI studies at lower angular resolutions. Future space VLBI missions and enhanced millimetre-wave global arrays, enabling high dynamic range observations capable to spatially resolving the jet width, should prove decisive in determining the true nature of jets powered by supermassive black holes.

Methods

Observations. Observations of 3C 279 (1253–055) were conducted at 22.2 GHz (1.3 cm) on 2014 March 10–11, spanning a total of 11:44 h from 14:15 to 01:59 UT. During the observing session, *RadioAstron* recorded evenly spaced (every 80–90 min) blocks of data of 30 min and one final block of ~ 2 h, corresponding to its orbit perigee. This allowed the spacecraft to cool down its high-gain antenna drive in between observing segments. Together with *RadioAstron*, a ground array of 23 antennas observed the target, namely ATCA (AT), Ceduna (CD), Hobart (HO), Korean VLBI Network (KVN) antennas Tanman (KT), Ulsan (KU), and Yonsei (KY), Mopra (MP), Parkes (PA), Sheshan (SH), Badary (BD), Urumqi (UR), Hartebeesthoek (HH), Kalyazin (KL), Metsähovi (MH), Noto (NT), Torun (TR), Medicina (MC), Onsala (ON), Yebes (YS), Jodrell Bank (JB), Effelsberg (EF), Svetloe (SV), and Zelenchukskaya (ZC).

Left and right circularly polarized signals (LCP and RCP, respectively) were recorded simultaneously at each station, with a total bandwidth of 32 MHz per polarization. Collected data were then processed at the Max-Planck-Institut für Radioastronomie using the upgraded version of the DiFX correlator ³⁹. Fringes between *RadioAstron* and ground stations were searched using the largest dishes, separately for each scan. This provides a first-order clock correction, to be later refined with baseline stacking in AIPS ⁴⁰. When no signal was found, we adopted a best-guess clock value extrapolated from scans giving fringes, with the aim of performing a further global fringe search at a later stage with AIPS.

Data reduction. For the initial data reduction, we made use of *ParseITongue* ⁴¹, a Python interface for AIPS. At a first stage, we performed an *a priori* calibration of the correlated visibility amplitudes using the system temperatures and gain curves registered at each station. Some of the antennas participating in the observations failed to deliver system temperature information, which we compensated by using nominal val-

ues modulated by the antenna’s elevation at each scan. Since we chose the average system temperature as the station’s default value, visibility amplitudes were not properly scaled. We overcame this issue by determining the gain corrections needed for each IF and polarization from a preliminary image where only closure-quantities (closure phases and log-closure amplitudes) were involved, using the software library *SMILI* ^{42,43}. The image total flux density was fixed to that measured by the intra-KVN baselines (27.65 Jy), whose *a priori* calibration was excellent. Finally, we corrected the phase rotation introduced by the receiving systems as the source’s parallactic angle changes.

We then solved for phase offsets and residual single-band delays by incrementally fringe-fitting the data. In the first iteration we excluded *RadioAstron* and performed a global fringe search on the ground array with a solution interval of 60 s, using MP and EF as reference antennas for the first and second part of the experiment, respectively. Once fully calibrated, the ground array was coherently combined to increase the signal-to-noise ratio of possible fringe detections to *RadioAstron*. To account for the acceleration of the spacecraft near its perigee and the low sensitivity of the longest projected baseline lengths to it, we adopted different solution intervals (from 10 s to 240 s) and data total bandwidth (by combining IFs and/or polarizations). With a signal-to-noise ratio cutoff of 5, reliable ground-space fringes were detected up to ~ 8 Earth’s diameters, corresponding to the first observing block of *RadioAstron* (around 14 UT), achieving a maximum angular resolution of $27 \mu\text{as}$ in the transverse direction to the jet axis. Lastly, we solved for the antennas’ bandpass, the delay difference between polarizations using the task RLDLY, and exported the frequency averaged data along each IF. The fringe-fitted visibility coverage in the Fourier plane is shown in Extended Data Fig. 1.

Imaging. Imaging of the data was carried out using novel regularized maximum likelihood (RML) methods ⁴⁴, implemented in the *eht-imaging* software library ^{17,18}. While the CLEAN algorithm ⁴⁵ has been widely used in the past for VLBI image reconstruction, novel RML methods are not extensively used, especially at centimetre wavelengths and space VLBI experiments. Generally speaking, RML methods try to solve for the image I that minimizes the objective function:

$$J(I) = \sum_{\text{data terms}} \alpha_D \chi_D^2(I, V) - \sum_{\text{reg. terms}} \beta_R S_R(I), \quad (3)$$

where α and β are hyperparameters that weight the contribution of the image fitting to the data χ^2 , and the image-domain regularization S , to the minimization of the previous equation. Contrary to traditional CLEAN, full closure data products (closure phases and log closure amplitudes) can be employed during image reconstruction in addition to complex visibilities, further constraining the proposed image. Given the large number of telescopes participating in the experiment, closure quantities have proven quite useful since atmospheric phase corruption and gain uncertainties are mitigated. Multiple regularization over the proposed image

can be imposed too, like smoothness between adjacent pixels or similarity to a prior image.

Prior to imaging, we first performed an initial phase-only self-calibration to a point source model with a solution interval of 5 s and coherently averaged the data in 120 s intervals, using the DIFMAP package⁴⁶. We compared these results with those obtained with the AIPS task CALIB, for which a signal-to-noise ratio cutoff of 5 was set, to ensure no artificial signal was introduced in the data. In the following paragraphs we describe the imaging procedure.

As a first step, we flagged all baselines to *RadioAstron* and imaged the data collected only by ground radio telescopes. The pre-processed data noise budget is inflated by a small amount (1.5%), to account for non-closing errors, and the image is initialized with an elliptical Gaussian, oriented in roughly the same angle as the 7 mm image and enclosed in a 1.5×1.5 mas field of view gridded by 200×200 pixels. As mentioned above, because of the poor *a priori* amplitude calibration due to missing antennas' system temperature, we opted for a first round of imaging where only closure quantities (closure phases and log closure amplitudes) were used to constrain the image likelihood. This likelihood takes the form of the mean squared standardized residual (similar to a reduced χ^2) as defined in ref.¹⁹. Each imaging iteration takes as initial guess the image reconstructed in the previous step blurred to the ground array nominal resolution, i.e. $223 \mu\text{as}$, which prevents the algorithm of being caught in local minima during optimization of Equation 3. We then self-calibrate the data to the closure-only image obtained and incorporate full complex visibilities to the imaging process, which is finalized by repeating the imaging and self-calibration cycle two more times. In addition to the data products mentioned, we impose several regularizations to the proposed images. These include maximum entropy (mem), which favors similarity to a prior image; total variation (tv) and total squared variation (tv2), which favor smoothness between adjacent pixels; ℓ_1 -norm, which favors sparsity in the image; and total flux regularization, which encourages a certain total flux density in the image. Finally, we restore all baselines to *RadioAstron* and repeat this procedure, substituting the Gaussian initialization with the blurred, ground-only image previously reconstructed and using the full array nominal resolution ($27 \mu\text{as}$) between imaging iterations to blur intermediate reconstructions.

Contrary to full Bayesian methods, RML techniques do not estimate the posterior distribution of the underlying image, but instead compute the maximum a posteriori solution, i.e. the single image that best minimizes Equation 3. The hyperparameters chosen will necessarily have an impact on the reconstructed image features, thus we conducted a scripted parameter survey to ensure the robustness of the subtle structures seen in Fig. 1 and to impartially determine which parameters perform better on the image reconstruction. From the many images obtained, we show in Extended Data Fig. 3 the complete collection of images which could potentially describe the observed source struc-

ture. These fit the data equally well and preserve the total flux measured by the KVN to a certain level. The regularizers and hyperparameters used to obtain these images are listed on each panel of Extended Data Fig. 3. Apart from these, we gave the same weight to complex visibilities and closure quantities data terms.

Polarimetric imaging. The polarization results presented in Fig. 1 were obtained using the `eht-imaging` library as well. A more complete description of the method can be found in refs.^{17,47}, here we briefly outline the procedure followed. For polarimetric imaging, `eht-imaging` minimizes again Equation 3, substituting complex visibilities and closure quantities data terms by polarimetric visibilities $\mathcal{P} = \tilde{Q} + i\tilde{U}$ and the visibility domain polarimetric ratio $\tilde{m} = \mathcal{P}/\tilde{I}$. Note that total intensity and linearly polarized intensity images are reconstructed independently. Image regularization includes now total variation which, as for total intensity imaging, encourages smoothness between adjacent pixels; and the Holdaway-Wardle regularizer⁴⁸, which prefers pixels with polarization fraction values below the theoretical maximum 0.75. The pipeline then alternates between minimizing the polarimetric objective function and solving for the complex instrumental polarization, the so-called D-terms. The instrumental polarization calibration is performed by maximizing the consistency between the self-calibrated data and sampled data from corrupted image reconstructions. After D-terms solutions are found for each antenna, the reconstructed polarimetric image is blurred, as was done for Stokes \mathcal{I} imaging, and the imaging-calibration cycle is repeated until convergence of the solutions.

Filament fitting. The relative right ascension and declination coordinates of the filaments were obtained from the fitting of three Gaussian curves to transverse profiles of the brightness distribution. We first computed the main jet axis, commonly referred to as ridge line, from a convolved version of the reconstructed image. Using a sufficiently large Gaussian kernel, we blurred our image until the emission blends into a unique stream and the filaments are no longer distinguishable, similarly to the 7 mm VLBA-BU-BLAZAR image. We then project this image into polar coordinates, centred at the jet origin, and slice it horizontally, storing the position of the flux density peak for each cut. These positions are then transformed back to Cartesian coordinates, obtaining thus the main jet axis. To each pair of consecutive points conforming the axis, we compute the local perpendicular line and retrieve the flux density of the pixels contained in the cut. With this procedure, we assemble a set of transverse brightness profiles to which we fit the sum of three Gaussian curves using the python package `lmfit`⁴⁹. The number of Gaussian components used is motivated by the number of filaments observed emanating from the core region, although we note that two Gaussian components are enough to fit the two main threads. Finally we select the coordinates as the position of the peak(s) found in the curve best fitting each cut.

Data availability

Data and other material presented in this paper are available from the corresponding author upon reasonable request.

Code availability

The software packages used to calibrate, image, and analyze the data are available at the following sites: AIPS (<http://www.aips.nrao.edu/index.shtml>), ParselTongue (<https://www.jive.eu/jivewiki/doku.php?id=parselftongue:parselftongue>), DIFMAP (<https://science.nrao.edu/facilities/vlba/docs/manuals/oss2013a/post-processing-software/difmap>), SMILI (<https://github.com/astrosmili/smili>), eht-imaging (<https://github.com/achael/eht-imaging>), and lmfit (<https://lmfit.github.io/lmfit-py/>).

References

1. Event Horizon Telescope Collaboration *et al.* First M87 Event Horizon Telescope Results. I. The Shadow of the Supermassive Black Hole. *Astrophys. J. Lett.* **875**, L1 (2019).
2. Jorstad, S. G. *et al.* Polarimetric Observations of 15 Active Galactic Nuclei at High Frequencies: Jet Kinematics from Bimonthly Monitoring with the Very Long Baseline Array. *Astron. J.* **130**, 1418–1465 (2005).
3. Lister, M. L. *et al.* MOJAVE: Monitoring of Jets in Active Galactic Nuclei with VLBA Experiments. V. Multi-Epoch VLBA Images. *Astron. J.* **137**, 3718–3729 (2009).
4. Kardashev, N. S. *et al.* “RadioAstron”—A telescope with a size of 300 000 km: Main parameters and first observational results. *Astronomy Reports* **57**, 153–194 (2013).
5. Kim, J.-Y. *et al.* Event Horizon Telescope imaging of the archetypal blazar 3C 279 at an extreme 20 microarcsecond resolution. *Astron. & Astrophys.* **640**, A69 (2020).
6. Marziani, P., Sulentic, J. W., Dultzin-Hacyan, D., Calvani, M. & Moles, M. Comparative Analysis of the High- and Low-Ionization Lines in the Broad-Line Region of Active Galactic Nuclei. *Astrophys. J. Suppl.* **104**, 37 (1996).
7. Maraschi, L., Ghisellini, G. & Celotti, A. A Jet Model for the Gamma-Ray-emitting Blazar 3C 279. *Astrophys. J. Lett.* **397**, L5 (1992).
8. Wardle, J. F. C., Homan, D. C., Ojha, R. & Roberts, D. H. Electron-positron jets associated with the quasar 3C279. *Nature* **395**, 457–461 (1998).
9. Abdo, A. A. *et al.* A change in the optical polarization associated with a γ -ray flare in the blazar 3C279. *Nature* **463**, 919–923 (2010).
10. Whitney, A. R. *et al.* Quasars Revisited: Rapid Time Variations Observed Via Very-Long-Baseline Interferometry. *Science* **173**, 225–230 (1971).
11. Cohen, M. H. *et al.* The Small-Scale Structure of Radio Galaxies and Quasi-Stellar Sources at 3.8 Centimeters. *Astrophys. J.* **170**, 207 (1971).
12. Hartman, R. C. *et al.* Detection of High-Energy Gamma Radiation from Quasar 3C 279 by the EGRET Telescope on the Compton Gamma Ray Observatory. *Astrophys. J. Lett.* **385**, L1 (1992).
13. Lister, M. L. *et al.* MOJAVE: Monitoring of Jets in Active Galactic Nuclei with VLBA Experiments. VI. Kinematics Analysis of a Complete Sample of Blazar Jets. *Astron. J.* **138**, 1874–1892 (2009).
14. Jorstad, S. G. *et al.* Kinematics of Parsec-scale Jets of Gamma-Ray Blazars at 43 GHz within the VLBA-BU-BLAZAR Program. *Astrophys. J.* **846**, 98 (2017).
15. Kovalev, Y. *et al.* Detection statistics of the radioastron agn survey. *Adv. Space Res.* **65**, 705–711 (2020). URL <https://www.sciencedirect.com/science/article/pii/S0273117719306180>. High-resolution space-borne radio astronomy.
16. Bloom, S. D., Fromm, C. M. & Ros, E. The Accelerating Jet of 3C 279. *Astron. J.* **145**, 12 (2013).
17. Chael, A. A. *et al.* High-resolution Linear Polarimetric Imaging for the Event Horizon Telescope. *Astrophys. J.* **829**, 11 (2016).
18. Chael, A. A. *et al.* Interferometric Imaging Directly with Closure Phases and Closure Amplitudes. *Astrophys. J.* **857**, 23 (2018).
19. Event Horizon Telescope Collaboration *et al.* First M87 Event Horizon Telescope Results. IV. Imaging the Central Supermassive Black Hole. *Astrophys. J. Lett.* **875**, L4 (2019).
20. Event Horizon Telescope Collaboration *et al.* First M87 Event Horizon Telescope Results. II. Array and Instrumentation. *Astrophys. J. Lett.* **875**, L2 (2019).
21. Planck Collaboration *et al.* Planck 2015 results. XIII. Cosmological parameters. *Astron. & Astrophys.* **594**, A13 (2016).
22. Nilsson, K., Pursimo, T., Villforth, C., Lindfors, E. & Takalo, L. O. The host galaxy of 3C 279. *Astron. & Astrophys.* **505**, 601–604 (2009).
23. Bardeen, J. M. & Petterson, J. A. The Lense-Thirring Effect and Accretion Disks around Kerr Black Holes. *Astrophys. J. Lett.* **195**, L65 (1975).
24. Morgan, C. W., Kochanek, C. S., Morgan, N. D. & Falco, E. E. The Quasar Accretion Disk Size-Black Hole Mass Relation. *Astrophys. J.* **712**, 1129–1136 (2010).

25. Mizuno, Y., Lyubarsky, Y., Nishikawa, K.-I. & Hardee, P. E. Three-dimensional Relativistic Magnetohydrodynamic Simulations of Current-driven Instability. III. Rotating Relativistic Jets. *Astrophys. J.* **757**, 16 (2012).
26. Perucho, M., Kovalev, Y. Y., Lobanov, A. P., Hardee, P. E. & Agudo, I. Anatomy of Helical Extragalactic Jets: The Case of S5 0836+710. *Astrophys. J.* **749**, 55 (2012).
27. Vega-García, L., Perucho, M. & Lobanov, A. P. Derivation of the physical parameters of the jet in S5 0836+710 from stability analysis. *Astron. & Astrophys.* **627**, A79 (2019).
28. Hardee, P. E. Spatial Stability of Jets: The Non-axisymmetric Fundamental and Reflection Modes. *Astrophys. J.* **313**, 607 (1987).
29. Hardee, P. E. On Three-dimensional Structures in Relativistic Hydrodynamic Jets. *Astrophys. J.* **533**, 176–193 (2000).
30. Aloy, M.-A., Gómez, J.-L., Ibáñez, J.-M., Martí, J.-M. & Müller, E. Radio Emission from Three-dimensional Relativistic Hydrodynamic Jets: Observational Evidence of Jet Stratification. *Astrophys. J. Lett.* **528**, L85–L88 (2000).
31. Fuentes, A., Gómez, J. L., Martí, J. M. & Perucho, M. Total and Linearly Polarized Synchrotron Emission from Overpressured Magnetized Relativistic Jets. *Astrophys. J.* **860**, 121 (2018).
32. Moya-Torregrosa, I., Fuentes, A., Martí, J. M., Gómez, J. L. & Perucho, M. Magnetized relativistic jets and helical magnetic fields. I. Dynamics. *Astron. & Astrophys.* **650**, A60 (2021).
33. Fuentes, A., Torregrosa, I., Martí, J. M., Gómez, J. L. & Perucho, M. Magnetized relativistic jets and helical magnetic fields. II. Radiation. *Astron. & Astrophys.* **650**, A61 (2021).
34. Rybicki, G. B. & Lightman, A. P. *Radiative processes in astrophysics* (1979).
35. Lyutikov, M., Pariev, V. I. & Gabuzda, D. C. Polarization and structure of relativistic parsec-scale AGN jets. *Mon. Not. R. Astron. Soc.* **360**, 869–891 (2005).
36. Lobanov, A. P. & Zensus, J. A. A Cosmic Double Helix in the Archetypical Quasar 3C273. *Science* **294**, 128–131 (2001).
37. Bruni, G. *et al.* RadioAstron reveals a spine-sheath jet structure in 3C 273. *Astron. & Astrophys.* **654**, A27 (2021).
38. Gómez, J. L. *et al.* Probing the Innermost Regions of AGN Jets and Their Magnetic Fields with RadioAstron. V. Space and Ground Millimeter-VLBI Imaging of OJ 287. *Astrophys. J.* **924**, 122 (2022).
39. Bruni, G. *et al.* The RadioAstron Dedicated DiFX Distribution. *Galaxies* **4**, 55 (2016).
40. Greisen, E. W. The Astronomical Image Processing System. In *Acquisition, Processing and Archiving of Astronomical Images*, 125–142 (1990).
41. Kettenis, M., van Langevelde, H. J., Reynolds, C. & Cotton, B. ParselTongue: AIPS Talking Python. In Gabriel, C., Arviset, C., Ponz, D. & Enrique, S. (eds.) *Astronomical Data Analysis Software and Systems XV*, vol. 351 of *Astronomical Society of the Pacific Conference Series*, 497 (2006).
42. Akiyama, K. *et al.* Superresolution Full-polarimetric Imaging for Radio Interferometry with Sparse Modeling. *Astron. J.* **153**, 159 (2017).
43. Akiyama, K. *et al.* Imaging the Schwarzschild-radius-scale Structure of M87 with the Event Horizon Telescope Using Sparse Modeling. *Astrophys. J.* **838**, 1 (2017).
44. Narayan, R. & Nityananda, R. Maximum entropy image restoration in astronomy. *Ann. Rev. Astron. Astrophys.* **24**, 127–170 (1986).
45. Högbom, J. A. Aperture Synthesis with a Non-Regular Distribution of Interferometer Baselines. *Astron. & Astrophys. Suppl. Ser.* **15**, 417 (1974).
46. Shepherd, M. C. Difmap: an Interactive Program for Synthesis Imaging. In Hunt, G. & Payne, H. (eds.) *Astronomical Data Analysis Software and Systems VI*, vol. 125 of *Astronomical Society of the Pacific Conference Series*, 77 (1997).
47. Event Horizon Telescope Collaboration *et al.* First M87 Event Horizon Telescope Results. VII. Polarization of the Ring. *Astrophys. J. Lett.* **910**, L12 (2021).
48. Holdaway, M. A. & Wardle, J. F. C. Maximum entropy imaging of polarization in very long baseline interferometry. In Gmitro, A. F., Idell, P. S. & Lahaie, I. J. (eds.) *Digital Image Synthesis and Inverse Optics*, vol. 1351 of *Society of Photo-Optical Instrumentation Engineers (SPIE) Conference Series*, 714–724 (1990).
49. Newville, M. *et al.* lmfit/lmfit-py: 1.0.3 (2021). URL <https://doi.org/10.5281/zenodo.5570790>.

Acknowledgements

We thank L. Hermosa for useful comments on the manuscript. The work at the IAA-CSIC is supported in part by the Spanish Ministerio de Economía y Competitividad (grants AYA2016-80889-P, PID2019-108995GB-C21), the Consejería de Economía, Conocimiento, Empresas y Universidad of the Junta de Andalucía (grant P18-FR-1769), the Consejo Superior de Investigaciones Científicas (grant 2019AEP112), and

the State Agency for Research of the Spanish MCIU through the “Center of Excellence Severo Ochoa” award to the Instituto de Astrofísica de Andalucía (SEV-2017-0709). JMM and MP acknowledge support from the Spanish *Ministerio de Ciencia* through grant PID2019-107427GB-C33, and from the *Generalitat Valenciana* through grant PROMETEU/2019/071. JMM acknowledges additional support from the Spanish *Ministerio de Economía y Competitividad* through grant PGC2018-095984-B-I00. MP acknowledges additional support from the Spanish *Ministerio de Ciencia* through grant PID2019-105510GB-C31. YYK was supported by the Russian Science Foundation grant 21-12-00241. AC is supported by Hubble Fellowship grant HST-HF2-51431.001-A awarded by the Space Telescope Science Institute, which is operated by the Association of Universities for Research in Astronomy, Inc., for NASA, under contract NAS5-26555. The *RadioAstron* project is led by the Astro Space Center of the Lebedev Physical Institute of the Russian Academy of Sciences and the Lavochkin Scientific and Production Association under a contract with the Russian Federal Space Agency, in collaboration with partner organizations in Russia and other countries. The European VLBI Network is a joint facility of independent European, African, Asian, and North American radio astronomy institutes. Scientific results from data presented in this publication are derived from the EVN project code GA030D. This research is partly based on observations with the 100 m telescope of the MPIfR at Effelsberg. This publication makes use of data obtained at Metsähovi Radio Observatory, operated by Aalto University in Finland. Our special thanks to the people supporting the observations at the telescopes during the data collection. This research is based on observations correlated at the Bonn Correlator, jointly operated by the Max-Planck-Institut für Radioastronomie, and the Federal Agency for Cartography and Geodesy. This study makes use of 43 GHz VLBA data from the VLBA-BU Blazar Monitoring Program (VLBA-BU-BLAZAR; <http://www.bu.edu/blazars/VLBAproject.html>), funded by NASA through the Fermi Guest Investigator grant 80NSSC20K1567.

Author contributions

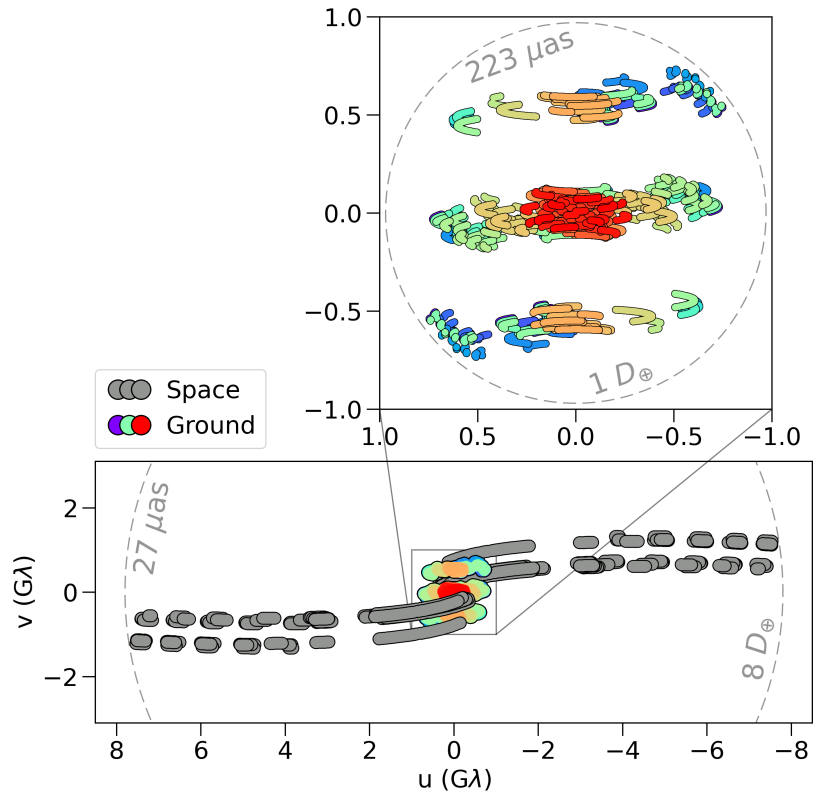
A.F., J.L.G., and G.Y.Z. worked on the data calibration. A.F., J.L.G., G.Y.Z., R.L., A.C., K.A., K.L.B., H.S., I.C, and E.T. worked on the image reconstruction and analysis. G.B. correlated the space VLBI data. J.M.M., M.P., A.F., J.L.G, and Y.M worked on the interpretation of the results. All authors contributed to the discussion of the results presented and commented on the manuscript.

Competing interests

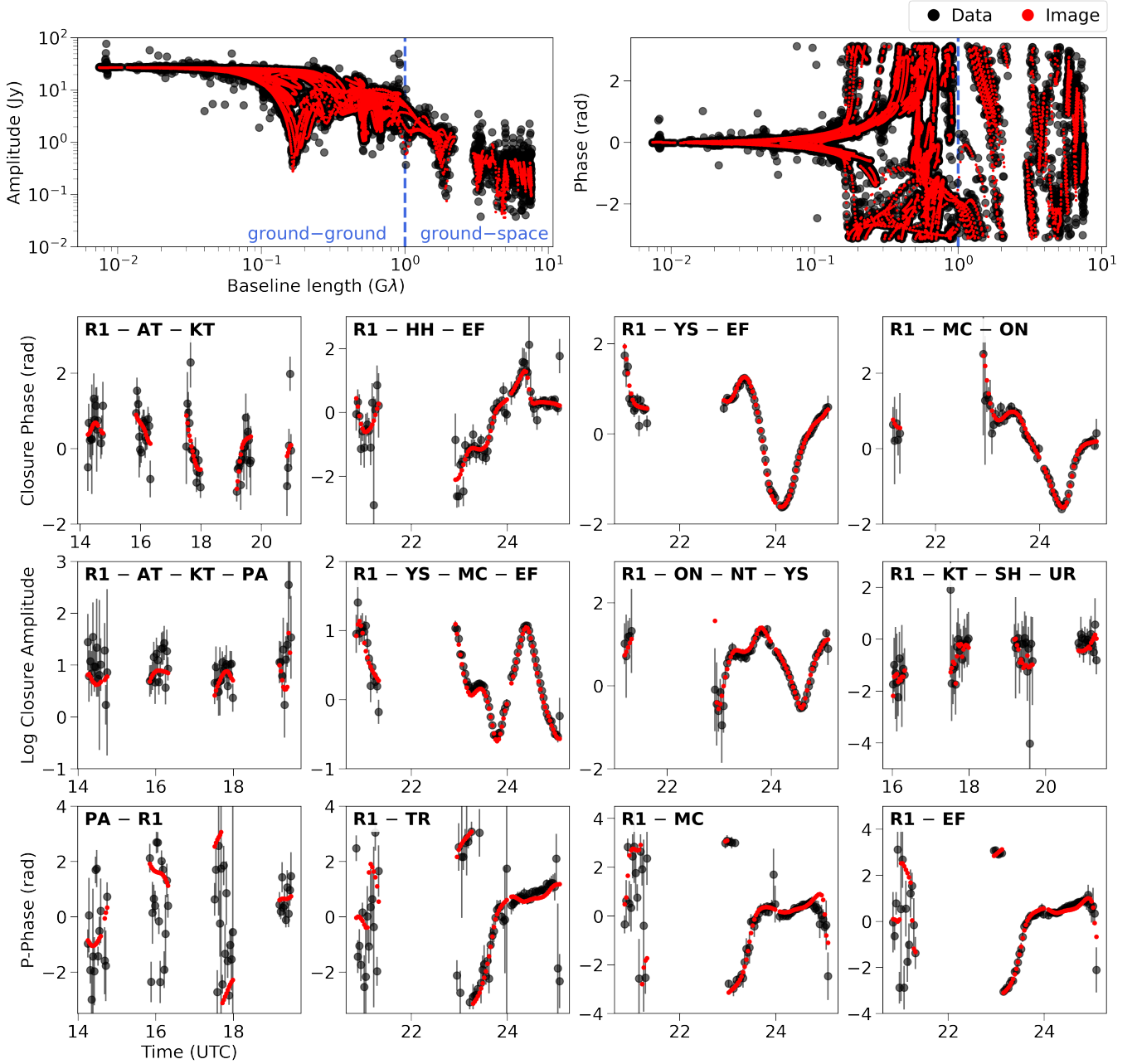
The authors declare no competing interests.

Additional information

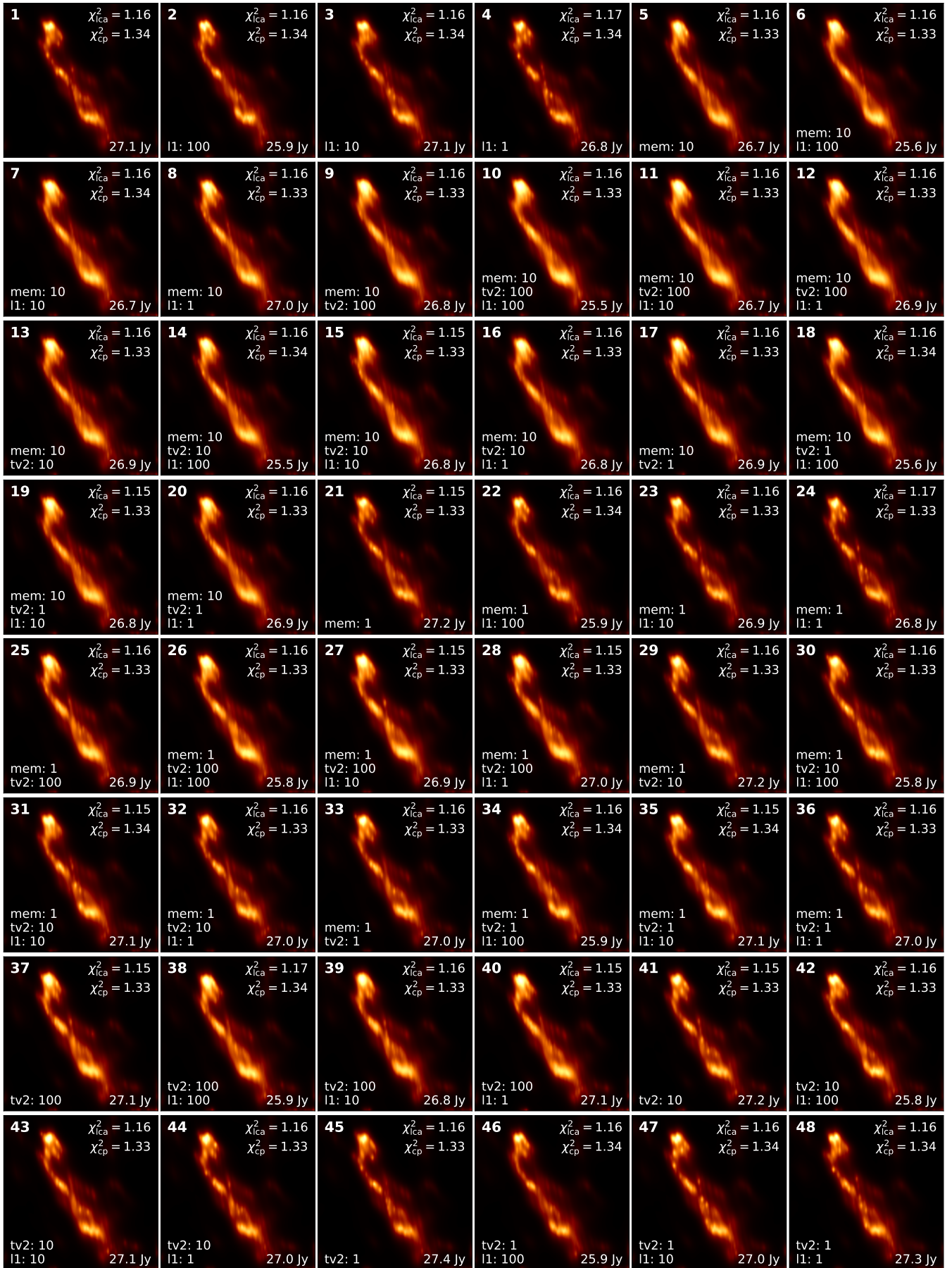
Correspondence and requests for materials should be addressed to A. Fuentes.



Extended Data Figure 1: Baseline coverage for our *RadioAstron* observations of 3C 279 in March 2014. Rainbow-coloured and grey points indicate individual ground-ground baselines and space-ground baselines, respectively. Dashed circles indicate the baseline length in Earth's diameter units (D_{\oplus}) and the corresponding angular resolution.



Extended Data Figure 2: Fitting of the polarimetric *RadioAstron* image to a selection of data products. Data (black points) and image model (red points) self-calibrated visibility amplitudes and phases, closure phases, log closure amplitudes, and polarimetric visibility phases as a function of time. All these examples include *RadioAstron* measurements.



Extended Data Figure 3: Top 48 image reconstructions from the parameter survey conducted. Each image includes the closure phase (cp) and log closure amplitude (lca) reduced χ^2 , the image regularizers used and their weight, and the total flux reconstructed. The image presented in Fig. 1 corresponds to #21, which has the overall minimum reduced χ^2 .